THE JOURNAL OF PHYSICAL CHEMISTRY A
A JOURNAL OF THE AMERICAN CHEMICAL SOCIETY

pubs.acs.org/JPCA

Article

Untangling the Efficient Boron-Initialized Hydroxyl-Terminated Polybutadiene Combustion for High Energetic Solid Propulsion Systems

Grace L. Rizzo, Souvick Biswas, Dongwon Ka, Xiaolin Zheng,* and Ralf I. Kaiser*

Cite This: *J. Phys. Chem. A* 2025, 129, 288−300

Read Online

ACCESS | Metrics & More | Article Recommendations | Supporting Information

ABSTRACT: Highly energetic boron (B) particles embedded in hydroxyl-terminated polybutadiene (HTPB) thermosetting polymers represent stable solid-state fuel. Laser-heating of levitated B/HTPB and pure HTPB particles in a controlled atmosphere revealed spontaneous ignition of B/HTPB in air, allowing for examination of the exclusive roles of boron. These ignition events are probed *in situ* via simultaneous spectroscopic diagnostics: Raman and infrared spectroscopy, temporally resolved high-speed optical and infrared cameras, and ultraviolet−visible (UV−vis) spectroscopy. The emission spectra unravel two stages of the B/HTPB ignition—the exoergic ignition of boron followed by HTPB combustion. It was found that HTPB readily absorbs the energy from the irradiating carbon dioxide (CO_2) laser but efficiently transfers that thermal energy to the densely arranged boron particles due to the lower heat capacity of the latter. This transferred energy causes a surge in temperature for the boron particles, leading to ignition (in an oxygen environment) in B/HTPB, unlike the case with HTPB alone. The accumulated energy from the second stage of boron ignition triggers the decomposition of HTPB in conjunction with hydrogen abstraction to produce radical precursors via boron oxides (BO and BO_2)—the key emitting intermediates detected. Along with conventional combustion products such as carbon dioxide (CO_2) and water (H_2O), the formation of partially oxidized gaseous products such as methanol (CH_3OH) and methyl vinyl ether have also been detected as a tracer of diverse oxidation events, suggesting a complex oxidation chemistry within HTPB and overall depict crucial insights for its use as a solid rocket fuel.

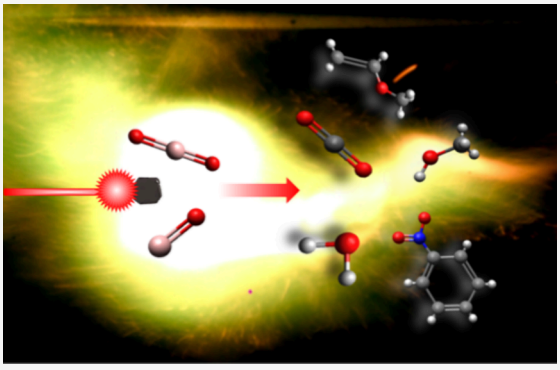

1. INTRODUCTION

Ever since Dr. Robert H. Goddard's pioneering work in 1915 on dramatically improving the efficiency of solid-fueled rockets from 2 to over 60%,[1] engine designers have continued to look for ways to meet the demands for ever-increasing fuel efficiency, seeking to launch heavier and faster payloads. In addition to the advancements in rocket motor design, improvements in the formulations of solid fuels are required to enhance the specific impulse, maintain thermal and mechanical stability, remain safe to handle, and produce fewer toxic byproducts. Throughout the years, major advances in propellant technology included the development of castable composites which consist of high-energy particles and a polymeric binder.[2,3] The most commonly used polymeric binder in solid rocket motor applications is hydroxyl-terminated polybutadiene (HTPB). HTPB is a preferred binder due to its low viscosity, high aging resistance, high specific impulse, and good mechanical properties at different temperatures.[2,3] With high volumetric and gravimetric energy densities (140 kJ cm^{-3}; 59 kJ g^{-1}),[2,4] boron (B) particles are attractive metal fillers for further improving the energy density of the composite solid fuels. When added to HTPB, boron has been shown to enhance the strength and stiffness of the HTPB matrix.[2,4] Additionally, in combustion, boron (5 wt % added to HTPB) was shown to increase the specific impulse (Isp) performance by 3.2% as compared to pure HTPB fuel.[5] Thus, adding boron to HTPB has been shown to promote an increase in the fuel mechanical properties, heat release, and combustion efficiency,[4−7] which is especially important for high-speed air-breathing propulsion systems such as solid fuel ramjets (SFRJ).[2,4,5,8] Prior to this work, the combustion and decomposition reaction mechanisms of boron particles and HTPB have both been studied individually for many years. The pyrolysis and decomposition of HTPB is a complex process with a diverse amount of products that have been discovered.[3] It has been shown that HTPB, under pyrolysis conditions (anywhere from 873 to 2000 K),[9,10] initially breaks down into smaller fragments as a result of C−C bond cleavage of the longer

Received: October 14, 2024
Revised: December 10, 2024
Accepted: December 11, 2024
Published: December 26, 2024

https://doi.org/10.1021/acs.jpca.4c06979
J. Phys. Chem. A 2025, 129, 288−300

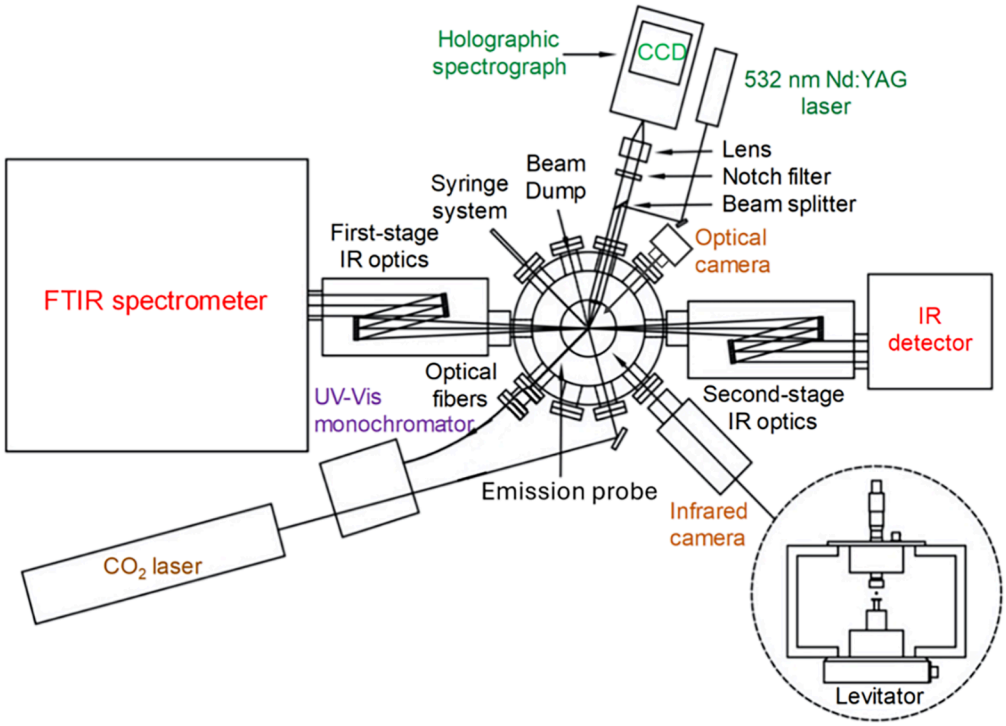

Figure 1. Schematic top view of the complete levitator apparatus displaying the ultrasonic levitator, process chamber, carbon dioxide laser, Raman spectrometer, infrared camera, optical camera, and some other complementary spectroscopy tools (FTIR spectrometer and fiber optic UV−vis spectrometer). Adapted with permission from ref 20. Copyright 2024 American Chemical Society.[14−20]

polymer chains.[9,10] These smaller fragments can either go on to form smaller stable molecules such as 1,3-butadiene (the most prominent gaseous product formed) and ethylene or undergo some cyclization and produce molecules such as toluene.[9,10] Extensive studies have been performed on the combustion of boron particles. Under high-temperature conditions, the combustion of boron follows a two-stage process. The first is the ignition stage where the removal of the oxide layer transpires (as low as 783 K; −69 kJ mol^{-1}).[11−13] The second stage is the combustion stage where the combustion of the boron core takes place (−461 kJ mol^{-1}).[12,13] This combustion process has been shown to yield important intermediate products such as boron dioxide (BO_2) and boron monoxide (BO).[12] Although the combustion of boron/hydroxyl-terminated polybutadiene (B/HTPB) has been recently studied,[5−8] there is still a lack of fundamental knowledge of the key reaction mechanisms that drive the combustion of B/HTPB.

Deciphering the efficiency of the complex combustion process and the underlying reaction mechanism of the B/HTPB composite fuel is essential to validate it as a superior fuel. From a chemical viewpoint, it is also imperative to decode the specific role of boron in the thermal decomposition and combustion of HTPB. This knowledge is also vital to the development of next-generation boron-based solid fuels and requires the identification of key reactive intermediates and transient species to depict the reaction mechanisms. Here, we report a comprehensive study of the thermal decomposition and ignition of singly levitated millimeter-sized B/HTPB composite particles via excitation of a quasi-continuous carbon dioxide (CO_2) laser under controlled conditions to resolve the mechanistic path while detecting reactive intermediates exploiting time-resolved ultraviolet−visible (UV−vis) emission spectroscopy and stable products released in the gas phase by Fourier Transform Infrared Spectroscopy (FTIR). The contactless levitation of such particles allows the elimination of higher-order surface-driven processes, which facilitates the study of the inherent reactivity of the particles. Primarily, small millimeter-sized levitating B/HTPB composite particles were studied within an ultrasonic levitator that is encapsulated in a stainless-steel process chamber. The chamber was filled with gases simulating both an inert atmosphere (100% argon (Ar)) and air (20% O_2 and 80% Ar mixture). Additionally, HTPB particles without boron were studied by using identical conditions to isolate the effects of boron in these reactions. Notably, the presence of boron in HTPB leads to spontaneous ignition with bright green-yellow flame, whereas no ignition was recorded for pure HTPB in simulated air (20% O_2 and 80% Ar mixture). Indicating strong catalytic influence from boron. From the flame emission spectroscopy, various key transient species such as boron dioxide (BO_2), boron (B), boron monoxide (BO), and diatomic carbon (C_2) were identified in the ignition of B/HTPB which cater as the vital information to reveal the boron mediated catalytic chemistry of the combustion event. Along with conventional combustion products such as carbon dioxide (CO_2) and water (H_2O), the formation of partially oxidized gaseous products such as methanol (CH_3OH) and methyl vinyl ether has also been detected as a tracer of diverse oxidation events. These key observations and systematic understanding of the complex combustion can then ultimately aid in the production of next-generation solid rocket and hydrocarbon fuels.

2. EXPERIMENTAL SECTION

2.1. Materials and Gases. Hydroxyl-terminated polybutadiene (HTPB) (RCS Rocket Motor Components Inc.) and isophorone diisocyanate (IPDI) (98%, Sigma-Aldrich) were used as a prepolymer and cross-linker, respectively. They were

https://doi.org/10.1021/acs.jpca.4c06979
J. Phys. Chem. A 2025, 129, 288−300

mixed in a stoichiometric ratio of 91.5%:8.5% (HTPB:IPDI) in mass by a speed mixer (FlackTek) at 2300 rpm for 3 min. The mixture was degassed in a vacuum; then, it was cured at 60 °C for 3 days. Amorphous boron powder (95% purity, SB Boron Corp.) was mixed with HTPB and IPDI to prepare B/HTPB. The mass percentage of B in B/HTPB is 30%. These particles were characterized using scanning electron microscopy (SEM; Thermo Fisher Scientific Apreo (TFS Apreo)) at a voltage and current of 10 kV and 50 pA, respectively. Particles were prepared by cutting larger samples into smaller millimeter-sized cubes. The largest particles that could be steadily levitated were approximately 3 mm in size. The argon (99.9999%, Ar) and oxygen (99.999%, O_2) used to fill the process chamber were obtained from Airgas.

2.2. Ultrasonic Levitator Apparatus. The experiments were carried out using an ultrasonic acoustic levitator. Ultrasonic sound waves were generated from a piezoelectric transducer oscillating at 58 kHz.[14−17] A standing wave is generated through multiple reflections between the transducer (bottom) and the concave reflector (top). The distance between the transducer and reflector is adjusted by a micrometer manipulator to an integral number of half wavelengths, which allows for resonance conditions to be maintained following any changes that occur in gas composition, temperature, or pressure. A typical distance between the front plate and reflector is selected to be 2.5 times the wavelength (14.8 mm), resulting in five pressure nodes. The amplitude of the oscillations can be optimized through an adjustment of the radio frequency (RF) power between 0.7 and 5.0 W and monitoring the feedback voltage on an oscilloscope. The levitator is housed within a pressure-compatible stainless-steel process chamber (Figure 1),[14−19] enabling HTPB and B/HTPB particles to be studied in a well-defined and contained, either pure argon or oxygen−argon environment at higher elevated pressures. The experiments were carried out at a pressure of 800 Torr, measured by a MKS 626B Baratron. 800 Torr was the optimal pressure to stabilize the particles in the third pressure node of the standing wave.

2.3. Solid Particle Sampling. Solid samples are levitated slightly below the pressure minima of the ultrasonic standing wave.[14−19] This is feasible since the acoustic radiation pressure from the sound waves counteracts the gravitational force. The horizontal restoring force centers the particle on the axis of the levitator. In the single-axis levitator, this horizontal force is 1 order of magnitude smaller than the axial force. The particles are introduced to the central pressure node via a magnetically coupled wobble stick attached to a side port of the process chamber. The 1 cm × 1 cm stainless-steel wire mesh is attached to the end of the wobble stick shaping an acoustically transparent spatula inside of the process chamber, which holds the HTPB and B/HTPB samples.[16,17]

2.4. Pyrolysis and Heating of Particles. To initiate the decomposition and ignition of the levitated particles, a 40 W carbon dioxide (CO_2) laser emitting at 10.6 μm (Synrad, Inc., model FSV40KFD) was used.[16,17] The output power of the laser can be adjusted by changing the duty cycle of the discharge by externally triggering the laser using a pulse delay generator (Quantum Composers 9518 plus). For the thermal decomposition experiment, the output is adjusted by 1% (0.5 W) per minute, reaching a maximum of 4% before the particles detrapped. Additionally, the CO_2 laser was operated in normal (laser running continuously) mode (Figure S1a). For the oxidation and ignition experiment, the output power of the laser was externally triggered and synchronized using the same pulse delay generator as described above. The CO_2 laser was operated in burst mode with a delay of 100 ms (Figure S1b) making it so the laser is only irradiated for a brief moment.[16,17] The overall duty cycle used in this experiment was 80% with a repetition rate of 1 kHz. For both experiments, the output of the laser passed through a zinc selenide window and was introduced to the center of the levitator by a parabolic copper mirror. The diameter of the laser beam was focused to a diameter of 0.2 mm onto the particle by using an 8-fold beam expander followed by a parabolic copper mirror with a focal length of 300 mm. The exiting beam from the laser had a diameter of 2.5 mm with a beam divergence angle of less than 7.0 mR.[16,17] The more or less cubic particles, due to their asymmetry compared to spherical particles, were found to be spinning around the vertical axis in the node of the sound wave; thus, the particles would have sufficient uniformity in heating.

2.5. Raman Spectroscopy. Raman spectroscopy is exploited to trace the chemical modifications of the trapped particle during the thermal decomposition experiment. The Raman transitions were excited by a 532 nm output of a diode-pumped, Q-switched Nd:YAG laser (CrystaLaser, model QL532−1W) at a repetition rate of 1 kHz. The laser operated with a beam diameter of 0.35 mm and a divergence angle of 3.8 mR, producing an average power output of 200 mW and a pulse width of 13.5 ns. After being reflected from a 45° mirror (Edmund Optics, model NT45−991, >99% reflectance) and a 45° dichroic beamsplitter (Semrock, RazorEdge, model LPD01−532RU-25 × 36 × 2.0), the laser beam entered the process chamber through an antireflection coated window.[17] A planoconvex lens with a focal length of 60 mm was exploited to focus the laser beam onto the particle. The lens then collimates the Raman-shifted photons backscattered from the levitated particles. The beam splitter reflects the incident 532 nm laser beam but transmits longer Raman-shifted wavelengths. These passed through a 532 nm RazorEdge ultrasteep long-pass edge filter (Semrock, model LP03- 532RE-25), which further decreased the transmitted 532 nm laser light. A 50 mm f/1.8 camera (Nikon, Nikkor 2137) lens focuses the light through the 100 μm entrance slit of the spectrograph; the resolution of the spectrometer is 9 cm^{-1}.[17]

The light then is introduced into a Holospec f/1.8 imaging spectrometer (Kaiser Optical Systems, model 2004500−501), where the beam is collimated by a lens toward two overlaid holographic transmission gratings (Kaiser Optical Systems, model Holoplex HPG-532). Each grating separates the Raman-shift wavenumbers into low and high regions (2400 to 100 cm^{-1}, 4000 to 2200 cm^{-1}). These gratings disperse the light onto spatially distinct halves of a Peltier-cooled charge-coupled device (CCD) detector (Princeton Instruments, PI-MAX2). The CCD detector is composed of 1024 × 256 pixels each having a pixel size of 26 μm. In order to reduce the fluorescence background, it is imperative to conduct pulsed Raman experiments with the pulsed laser and the gated detector system described above. The time delay between the laser pulse, the opening gate to collect signal, and the period for which the gate is open are optimized to allow for an early detection of the Raman signal while rejecting the major portion of the "delayed" fluorescent background. Here, the HTPB particles produced a significant amount of fluorescence. To help this, the CCD was kept at a pulse width of 50 ns per pulse and a gate delay of 490 ns with 1000 gates per exposure. The detector operated at a 1 kHz repetition rate. Both the excitation laser and the detector were

https://doi.org/10.1021/acs.jpca.4c06979
J. Phys. Chem. A 2025, 129, 288−300

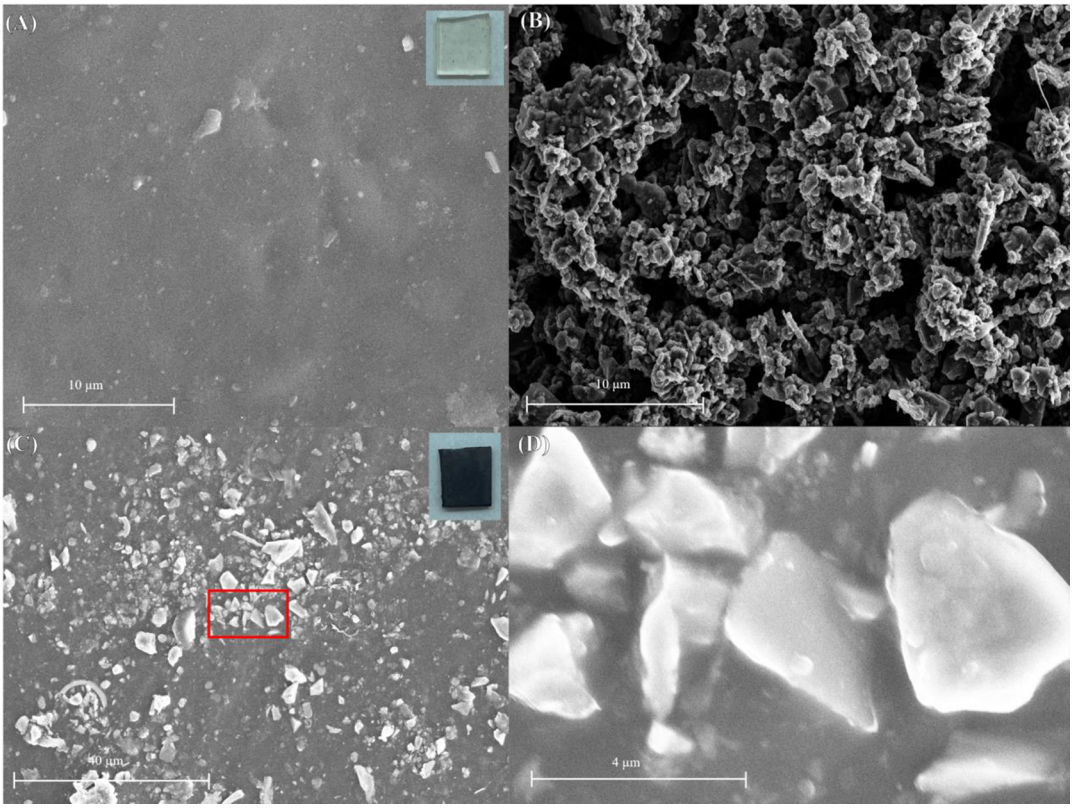

Figure 2. (A) SEM image of HTPB without boron particles. The inset displays the HTPB polymer at full scale. (B) SEM image of the isolated boron particles. (C) SEM image of the boron particles within the HTPB matrix. The inset displays the B/HTPB polymer at full scale. (D) Magnified SEM image of the boron particles in (C) outlined in red.

externally triggered through the pulse delay generator as described above (Figure S1a).

2.6. Fourier Transform Infrared (FTIR) Spectroscopy. The gases produced by the thermal decomposition and ignition of the HTPB and B/HTPB were detected by collecting an FTIR spectrum in the 400−4000 cm^{-1} wavenumber region through the full width of the process chamber. The FTIR spectrometer system combines a Nicolet 6700 FTIR spectrometer (Thermo Scientific) with two stages of copper mirror optics. The infrared incident beam from the spectrometer was focused into a diameter of 4 mm around the levitated sample before recollimating prior to detection by a liquid nitrogen-cooled MCT-B (mercury cadmium telluride, wide band) detector. The accumulation time for each spectrum was 1 min with a spectral resolution of 4 cm^{-1}. In the experiment, data acquisition was initiated at the start of heating. For the thermal decomposition experiment, the data collection was accumulated continuously from the start of heating until after the particles decaptured at the end of heating to observe the production of gaseous products. The background infrared spectrum was recorded each time before loading the particles.

2.7. Ultraviolet−Visible Spectrometer. The ultraviolet−visible (UV−vis) spectra were collected *in situ* in the wavelength region of 200 to 1,100 nm using a StellarNet SILVER-Nova zAP1 UV−vis spectrometer with a fiber optic probe (high OH fused silica core; 200−1100 nm).[16] The end of the fiber optic probe is attached to an x, y, and z manipulator to position the receiving end of the probe at an optimal distance from the ignition. In this experiment, the end of the probe was positioned 13 mm from the center of the levitator. For every measurement, the UV−vis spectrometer operated at a 1 kHz rate, collecting 127 consecutive spectra. The detector integration time was set to 2 ms. The UV−vis spectrometer was externally triggered and synchronized to the CO_2 laser with a delay of 100 ms (Figure S1b). The wavelength-dependent sensitivity calibration for the spectrometer system, including the optical fiber, has been performed prior to the experimental run, and the methods are briefly outlined in previous studies.[16] To account for the baseline shape and sample emissivity, the modified Planck's blackbody radiation formula (eq 1) is used to account for the $1/\lambda$ wavelength dependence of emissivity.[15]

$$E(T, \lambda) = \varepsilon(T, \lambda)\frac{2\pi hc^2}{\lambda^5}\frac{1}{e^{(hc/\lambda k_B T)} - 1} = \frac{C(T)}{\lambda^6}/(e^{hc/\lambda k_B T} - 1) \quad (1)$$

where $\varepsilon(T, \lambda)$ is emissivity, h is Planck's constant, k_B is Boltzmann's constant, c is the speed of light in vacuum, T is temperature, λ is the wavelength and $C(T)$ is a numerical fit constant that includes temperature dependence on emissivity.[15] In addition, varying the $\sin(2\pi n\lambda/\lambda_r)$ and $\cos(2\pi n\lambda/\lambda_r)$ functions are added to the baseline to adjust for unaccounted wavelength dependencies of emitting particles.[15] Since the samples do not show perfect blackbody radiation, the emissivity is not equal to unity and therefore can be treated as gray body radiation.

2.8. Optical and Infrared Videos. Optical videos were obtained by a Phantom Miro 3a10 camera equipped with a Navitar Zoom 6000 modular lens system. Infrared thermal imaging videos were collected in tandem with the optical videos using an FLIR A6703sc IR camera. For the thermal

https://doi.org/10.1021/acs.jpca.4c06979
J. Phys. Chem. A 2025, 129, 288−300

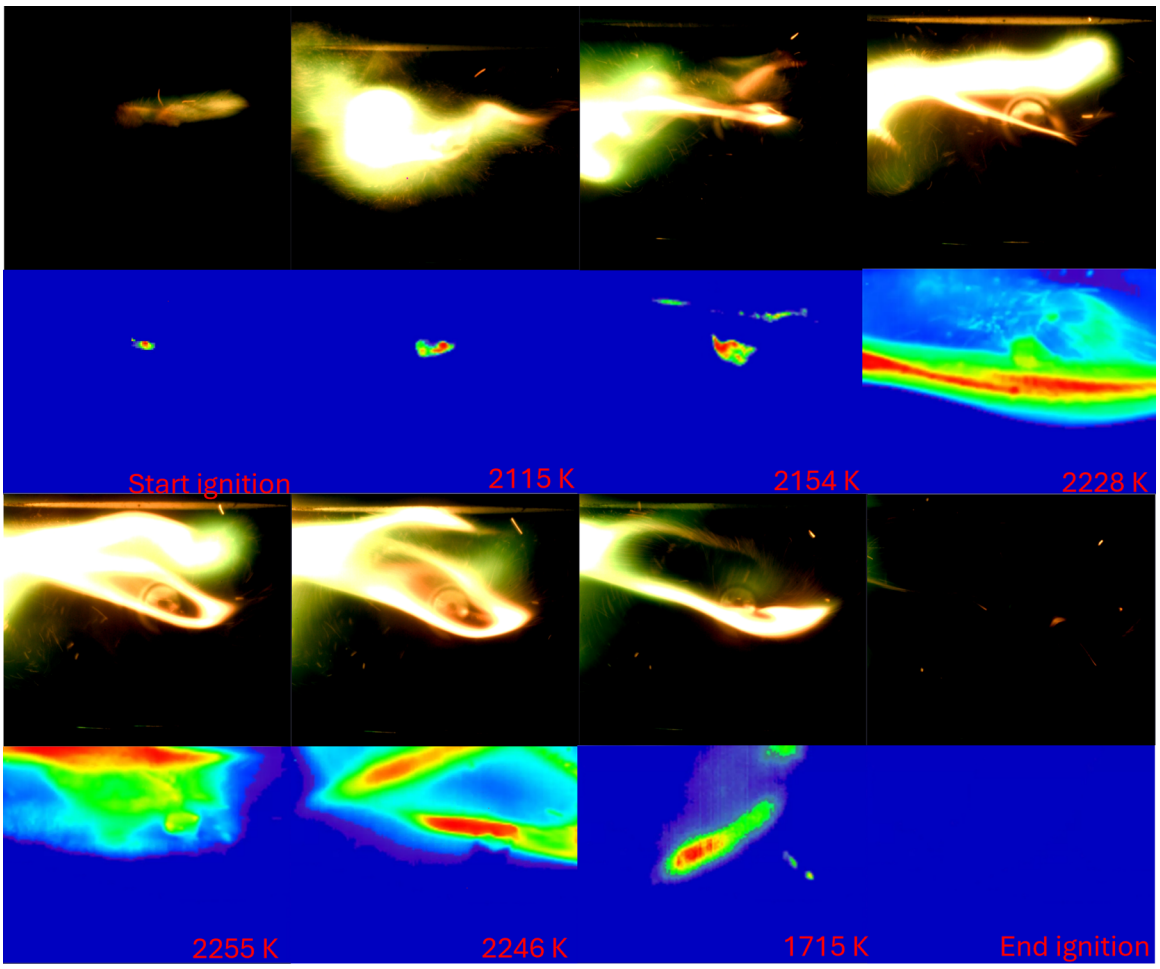

Figure 3. Optical and Infrared camera images of B/HTPB ignited in 20% O_2 and 80% Ar.

decomposition experiment, both cameras were triggered internally and operated at a frame rate of 30 Hz. These cameras could be operated at higher repetition rates; however, 30 Hz was used for optimized synchronization and to allow for the recording of longer movies. To capture the ignition event of B/HTPB, the optical camera was operated at 1 kHz. An ND2 filter was used to attenuate the intensity while working in the high-temperature range (523−1773 K). The infrared (IR) camera was set to a repetition rate of 250 Hz. Both cameras were externally triggered by the pulse delay generator without any delay referenced to the trigger pulse (Figure S1b).

3. RESULTS

3.1. Material Characterization. The detailed preparation methods for HTPB and the B (30 wt %)/HTPB composites are discussed in the experimental section. The cured HTPB (Figure 2a) has a clear color with a smooth surface and a rubbery texture. The B particles used here have irregular shapes with sizes ranging from submicrometer to a few micrometers. The B/HTPB sample has a dark color with numerous B particles scattered in the HTPB matrix (Figure 2c,d).

3.2. Optical and Infrared images. To capture any changes in the HTPB and B/HTPB particles during heating by a CO_2 laser followed by ignition, high-speed, synchronized optical, and infrared (IR) videos were utilized (Supporting Information movies M1−M4 and M1IR−M4IR). Extracted snapshots of the ignition of B/HTPB in a 20% O_2 and 80% Ar mixture are displayed in Figure 3. The snapshots for the heating of HTPB and B/HTPB in 100% Ar and 20% O_2/80% Ar are compiled in Figures S2−S4. Temperatures are determined using the infrared camera and corrected with the gray body temperatures found from the UV−vis. The temperatures obtained from the UV−vis were found using previous procedures.[15] Uncertainty for the temperatures is based on both the fluctuations in the IR camera and the fitting of the emission spectra.[15]

During the ignition of B/HTPB in 20% O_2 and 80% Ar (Figure 3), two distinct stages can be noted. The first stage is the ignition of the boron particles with the generation of a bright flash of green flame, and the second is the ignition of HTPB which exhibits more of an orange flame. During the first stage of ignition, there is a rapid rise in temperature to 2,115 ± 59 K which continues rising until a maximum of 2,255 ± 59 K is reached. Under the same conditions, HTPB without boron burns with no signs of ignition (Figure S2). However, there is a release of dense smoke at the maximum temperature of 877 ± 10 K. After heating, the HTPB particle volume is significantly reduced by 50% of its original volume and appears to have a smooth, reflective surface.

To examine the thermochemical and thermophysical changes of B/HTPB in the inert atmosphere (100% Ar), the particles were heated from room temperature (300 K) until the particles detrap at about 1168 ± 10 K (Figure S3). Initially, there is not much visible change, but later, white smoke is released from the hot particle when the temperature reaches 1027 ± 10 K. At the

https://doi.org/10.1021/acs.jpca.4c06979
J. Phys. Chem. A 2025, 129, 288−300

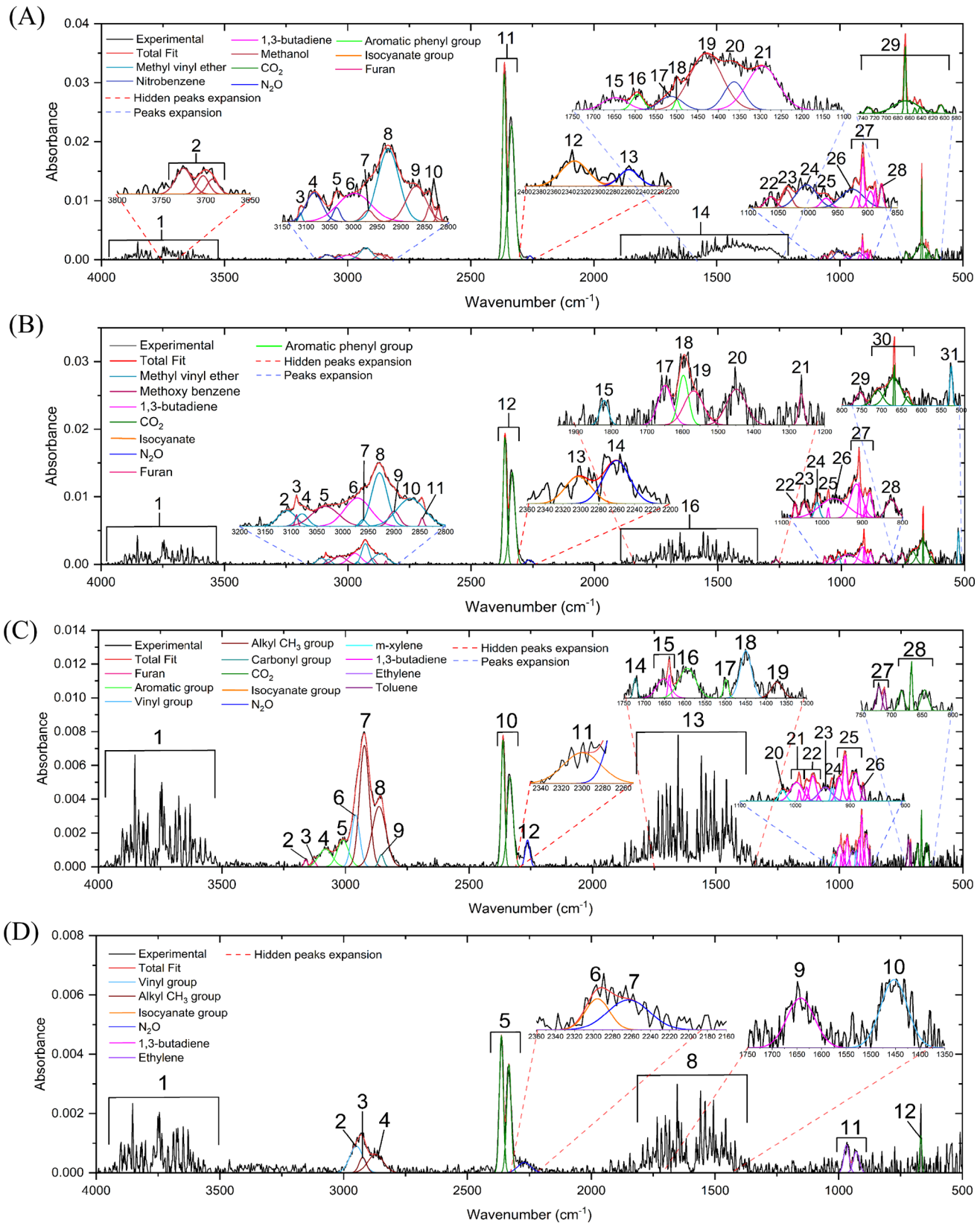

Figure 4. Deconvoluted gas phase FTIR spectra of HTPB and B/HTPB after heating in both 100% Ar and 20% O_2/80% Ar. Panels (A) and (B) are the spectra of B/HTPB and HTPB in 20% O_2, respectively. Panels (C) and (D) are the spectra of B/HTPB and HTPB in 100% Ar, respectively. See Tables S4−S7 for peak assignments.

maximum temperature (1168 ± 10 K), the particle shows a remarkable (approximately 70%) decrease in volume. In comparison, when HTPB is heated under the same conditions, first, the breakdown of the polymer via a yellow discoloration

https://doi.org/10.1021/acs.jpca.4c06979
J. Phys. Chem. A 2025, 129, 288−300

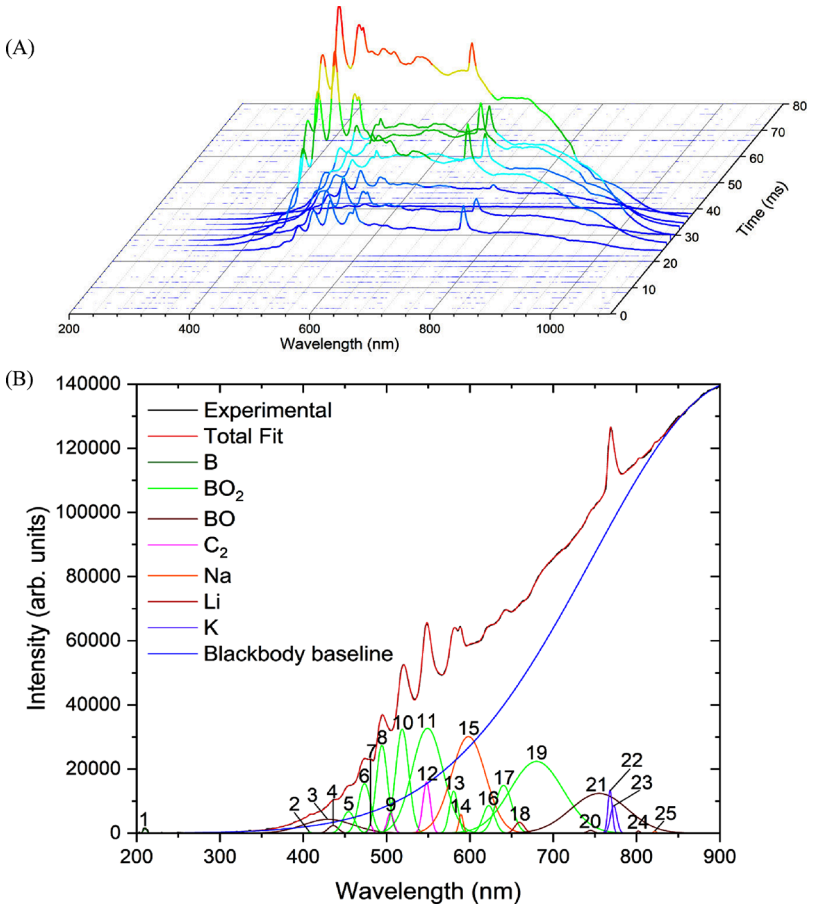

Figure 5. (A) 3D plot of the B/HTPB emission spectra when levitated in 20% O_2 and 80% Ar. (B) Deconvoluted most intense UV−vis emission spectrum from (A). See Table S8 for peak assignments.

and a shiny surface at 587 ± 10 K is observed (Figure S4), which is followed by the shattering of the particle into several smaller pieces, accompanied by a small release of gas at 718 K ± 10 K. Visibly, the amount of generated gas is much less than with boron present. Additionally, it appears that with boron, the particle achieves much hotter temperatures than without boron, which can be corroborated to boron having a lower specific heat capacity (1.05 J g^{-1} K^{-1}) than HTPB (approximately 2.5 J g^{-1} K^{-1}).[21−23] This would overall lower the heat capacity, implying that it would take less energy to raise the temperature of B/HTPB than HTPB to a given temperature.

To depict the chemical changes of heated HTPB in situ, simultaneously Raman spectroscopy was utilized starting from room temperature (300 K) to the different transition temperatures during decomposition, i.e., at 587 and 718 K (Figure S5a,b). At room temperature, the most intense features can be attributed to the polymeric chains of HTPB as well as features from the urethane bonds formed from the curing agent, isophorone diisocyanate (IPDI) (Figure S6 and Table S1).[24−26] As the temperature approaches 587 K, conversion from polymeric chains to aromatic compounds within the HTPB matrix is evident, which can be seen in the large background fluorescence. The spectral deconvolution revealed the major aromatic compounds to be toluene and *m*-xylene (Figure S7 and Table S2).[24−28] Once the temperature reached 718 K, the Raman spectra indicated a dominating presence of aromatic compounds (Figure S8 and Table S3)[24−28] within the levitating particle along with smaller alkenes such as 1,3-butadiene. Recall that at this temperature, the particles shatter and gas is released, which were investigated by complementary FTIR spectroscopy. The presence of boron in B/HTPB significantly enhances light absorption, leaving no detectable Raman scattering; thus, B/HTPB was unable to be characterized using Raman spectroscopy.

3.3. FTIR Spectra of the Gas Phase Products. The deconvoluted gas phase FTIR Spectra for the decomposed products of HTPB and B/HTPB in 100% Ar and 20% O_2 are shown in Figure 4. All assignments for peaks found in Figure 4 can be found in Tables S4−S7.[25−43] Each spectrum taken is at the maximum temperature in each heating process. When heated in 20% O_2 and 80% Ar, there are ample oxidized gaseous products seen in both HTPB and B/HTPB. It is worth noting that HTPB combustion has a plethora of gaseous products that form. Here, generalized assignments have been made. However, there are some distinct features that have helped in identifying a handful of molecules that form, adding to previous mass spectrometric and FTIR studies for the thermal degradation/combustion of the pure HTPB.[3,9,10,31,33,44] The most notable features correspond to the asymmetric, symmetric, and bending vibrations from both gaseous water (4000−3500 cm^{-1}; 2000−1400 cm^{-1}) and carbon dioxide (2363 cm^{-1}; 668 cm^{-1}). In the high-wavenumber region, several symmetric and asymmetric C−H stretches (3113−3034 cm^{-1}) are apparent. It is plausible that these are developed from the oxidized species methyl vinyl ether from B/HTPB combustion (Figure 4a). Additionally, features of 1,3-butadiene (symmetric stretch of vinyl CH_2 group;

https://doi.org/10.1021/acs.jpca.4c06979
J. Phys. Chem. A 2025, 129, 288−300

2998 cm^{-1}) and methanol (symmetric C−H stretch; 2868 and 2840 cm^{-1}) are also present. Also, multiple aromatic C−H asymmetric and symmetric stretches can be linked with furan and nitrobenzene (3112, 3082, and 3035 cm^{-1}) and other species. The OH stretch of methanol was found at 3705 cm^{-1}. From the 2400 to 2200 cm^{-1} region, there are two distinct bands characteristic of the asymmetric stretch of an isocyanate group (2332 cm^{-1}; R−N═C═O) and the asymmetric stretch of nitrous oxide (N_2O; 2260 cm^{-1}). There is a rise in broad features from 1600 to 1200 cm^{-1}, which consists of the CH_3 bending mode from methanol (1430 cm^{-1}) and NO_2 asymmetric and symmetric stretches from nitrobenzene (1514 and 1363 cm^{-1}), as well as the bending vibration of water vapor. The presence of 1,3-butadiene and methyl vinyl ether is confirmed by locating its C═C stretching vibration at 1648 cm^{-1}. The peaks located at 1594 and 1500 cm^{-1} are associated with the C═C and C−C stretches from the aromatic rings. Looking at the fingerprint region (1200−500 cm^{-1}), most of the features belong to the C−H bending vibrations from 1,3-butadiene (1295, 971, and 908 cm^{-1}). Additional C−H stretches arise from the aromatic rings of furan and nitrobenzene (1062 and 934 cm^{-1} respectively). Finally, at 1035 cm^{-1}, the stretching vibration of the C−O bond in methanol is observed.

When comparing HTPB in 20% O_2, the products methyl vinyl ether, furan, 1,3-butadiene, isocyanate group, CO_2, gaseous water, and N_2O are also present (Figure 4b). Although methanol and nitrobenzene are not observed, there are new symmetric and asymmetric C−H stretches (3090, 3034, 2900, 2846 cm^{-1}) from methoxybenzene, which also exhibits several new C−H bending vibrations (828 and 754 cm^{-1}).

Even in the absence of O_2, the products furan, 1,3-butadiene, isocyanate group, CO_2, gaseous water, and N_2O are seen in the heating of B/HTPB and HTPB in 100% Ar with the exception of furan in HTPB alone (Figure 4c,d). This indicates an active oxidation chemistry induced by the constituent oxygen (O) atoms in HTPB. In B/HTPB (Figure 4c), new C−H asymmetric and symmetric stretches and bending vibrations arise that evolve from the aromatic species m-xylene and toluene (3084, 3011, 1017, 876, and 721 cm^{-1}). Additionally, C−H vibrations are associated with the asymmetric stretch of the vinyl CH_2 group (2959 cm^{-1}) plausibly originating from 1,3-butadiene and ethylene. Also, there are asymmetric and symmetric stretches of an alkyl CH_3 group (2923 and 2863 cm^{-1}) found in this region. The feature at 1721 cm^{-1} can be assigned as the C═O stretch that originates from the urethane bond.[33,45] Lastly, two new peaks located at 876 and 721 cm^{-1} are found to be associated with the C−H bending vibrations of toluene and *m*-xylene. Recall that 1,3-butadiene, toluene, and *m*-xylene were all identified in the Raman spectra of HTPB decomposition, implying in situ thermal chemistry in the solid matrix. In the decomposition of HTPB in 100% Ar (Figure 4d), no signature of aromatic compounds was detected. Only the species listed above and ethylene were identified. Carbon dioxide (CO_2) and water (H_2O) vapor were the most common gaseous products produced from both HTPB and B/HTPB in 100% Ar and 20% O_2. In all cases, almost double the amount of CO_2 and gaseous water is produced by B/HTPB compared to HTPB alone.

3.4. Flame Emission (UV−vis) Spectroscopy. Temporally resolved UV−vis emission spectra are important tools for the detection of intermediates formed during the ignition (oxidation) process. A characteristic set of emission spectra acquired for the ignition of B/HTPB particle is displayed in Figure 5. The ignition starts 22 ms after the first pulse of the CO_2 laser (ignition delay) in which the ignition lasted for 20 ms with the most intense emissions occurring 28 ms into the first stage of the ignition (Figure 5a).

Several emitting open- and closed-shell species that are formed during the ignition are detected by this technique. Electronic transitions are assigned from the gray body-corrected deconvoluted spectral trace as displayed in Figure 5b. The resulting peak assignments have been compiled in Table S8.[14,15,18,46] The most dominant emission features are linked to the open shell diatomic radical boron dioxide (BO_2; X $^2\Pi g$). The strongest of these emissions is associated with the transition A $^2\Pi u$ − X $^2\Pi g$ at 548 nm. Additional weaker diatomic radical emission evolves from boron monoxide (BO; X $^2\Sigma^+$). The strongest emission is connected to transition A $^2\Pi$−X $^2\Sigma^+$ at 755 nm. In addition to these radicals, several atomic emissions were observed, such as boron (B; $^2P_{1/2}$), identified by its characteristic $2p^2\ ^2D - 2p\ ^2P^\circ$ transition located at 210 nm. Atomic emissions from the impurities: sodium (Na; $3p\ ^2P^\circ - 3s\ ^2S$, 589 nm), potassium (K; $4p\ ^2P^\circ - 4s\ ^2S$, 768), and lithium (Li; $2p\ ^2P^\circ - 2s\ ^2S$, 660 nm) also appear in the spectral trace. Diatomic carbon (C_2; a $^3\Pi u$) is also detected from its four emission peaks associated with the swan transition d $^3\Pi g$−a $^3\Pi u$; the strongest one being 549 nm.

Consistent with the camera images, two ignition stages are also observed spectroscopically (Figure S9). Recall that during the first stage, the boron particles are ignited, and there is a bright green flame. This observation is confirmed by the enhanced emission intensity of the BO_2 features between 22 and 30 ms. With the progress of the ignition, (beyond 32 ms) there is a notable shift in the gray body curve and a decrease in the intensity of the BO_2 and BO peaks which can be seen in the deconvoluted second stage spectrum (Figure S10 and Table S9).[14,15,18,46] On the contrary, the C_2 peaks are increased in intensity in the second stage of ignition.

The temporal evolution of selected peaks from all species is obtained from the emission spectrum. Looking at the most prominent species in the emission spectrum (C_2, BO, BO_2), the temporal profiles follow the trend of the two stages in the ignition (Figure S11). It can be seen that BO_2 has the greatest overall intensity. Across all three species, the peaks generally follow the same trends, with no major differences. The intensities spike to a maximum intensity at 26 ms, followed by a drop in intensity at 30 ms. There is another increase in intensity for the majority of the peaks at 32 ms, indicative of the second stage of the ignition. The only notable differences can be seen in a couple of peaks (744 and 802 nm) from the BO. For these peaks, there is a delayed spike in intensity starting at 24 ms. For the atomic boron peak and the peaks for the impurity species (Na, K, and Li), the temporal evolutions can be found in Figures S12−S17.

From the emission spectrum, the gray body temperature is plotted to observe the temperature changes over time. Uncertainty was based on the fitting of the temperatures with the emission spectra.[15] This gray body temperature profile is compared to the vibrational temperature profiles of C_2, BO, and BO_2 (Figure 6). The vibrational temperatures are calculated using the same equations and procedures as described in previous studies.[14] Uncertainty was determined from the initial intensity measurements that is propagated through the temperature calculation.[14] To start, the gray body temperature obtained from the experiment must first be established. The maximum gray body temperature reached during the ignition was 2255 ± 59 K. Here, it can be seen that BO rises to a maximum

https://doi.org/10.1021/acs.jpca.4c06979
J. Phys. Chem. A 2025, 129, 288−300

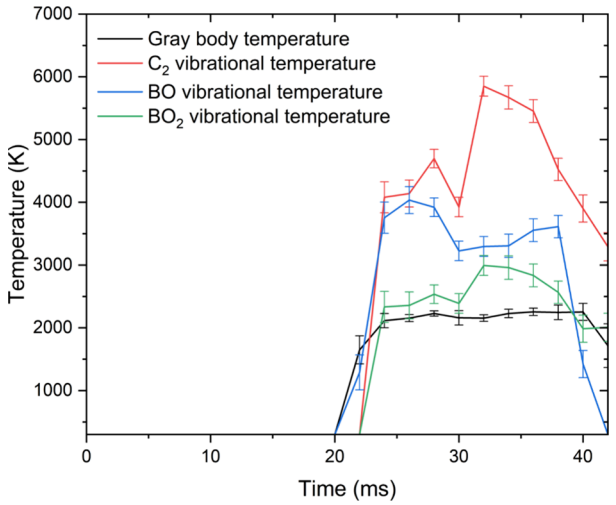

Figure 6. Temperature plot of the experimental (gray body) and vibrational temperatures of selected species (C_2, BO, and BO_2) during ignition of B/HTPB when levitated in 20% O_2 and 80% Ar.

vibrational temperature of 4035 ± 158 K in the initial stage at 26 ms. For C_2, there is a spike in temperature to 5850 ± 158 K at 32 ms. This is the maximum temperature reached for C_2 and the highest vibrational temperature reached overall between the species. The vibrational temperatures obtained for BO_2 closely follow the temperatures obtained for the gray body temperature. The maximum temperature reached for BO_2 is 2993 K ± 158 K at 32 ms.

4. DISCUSSION

Here, the specific role of boron in the thermal decomposition and oxidation of HTPB was deciphered by using various complementary time-resolved techniques. Utilizing high-speed optical and infrared imaging, the captured images revealed that there are two distinct stages in the ignition of B/HTPB in 20% O_2. The first is the ignition of the boron particles, and the second is the initiation of the burning of HTPB. It can be inferred that the burning of HTPB is initiated by the ignition of the boron particles as under the same conditions, HTPB does not ignite without the boron particles (Figure S2) which is due to, as stated above, boron having a two-stage ignition.[13,47] It was found that the ignition stage (first stage) of boron has a relatively short combustion time lasting between 1 and 3 ms (depending on the particle size and oxygen content),[13,47] significantly less than that of the combustion stage (second stage) where it can have a combustion time upward of 16 ms.[47] Knowing that this stage releases significantly more energy (−461 kJ mol^{-1}),[13] it can be concluded that the second stage of boron drives the ignition of HTPB. Under ambient conditions, B/HTPB burns at temperatures exceeding 1168 K, and more smoke is produced (Figure S18), which helps to stabilize HTPB. HTPB has been shown to absorb well in the same Infrared region as the CO_2 laser (1000−946 cm^{-1}) more than that of boron particles with the oxide layer.[33,48,49] Thus, HTPB would absorb more of the energy but because boron has a lower specific heat capacity (1.05 J g^{-1} K^{-1}),[21−23] this absorbed energy would quickly be distributed to the densely arranged boron particles causing them to increase in temperature and even ignite in the presence of oxygen (783 K).[11] Since, as seen above, the particles are well dispersed throughout the HTPB matrix, which would help distribute even heating throughout HTPB ultimately resulting in increased temperatures and reaching a maximum temperature of 2255 ± 59 K, which initiates the ignition of HTPB. This increased temperature also qualitatively explains why there was a production of more smoke and hotter temperatures in the case of B/HTPB.

The FTIR reveals several oxidized and nonoxidized gaseous products formed during combustion and heating of B/HTPB and HTPB in 20% O_2 and 100% Ar. It is observed that in both the 20% O_2 and 100% Ar cases, there are increased vibrational features of the aromatic and small alkene products from the B/HTPB than as seen in the HTPB alone. It is also observed that boron increases the production of CO_2 as evident from the comparison of the corresponding FT-IR spectra. This observation is in conjunction with the fact that more smoke is produced with B/HTPB than with HTPB alone (Figure S18).

From the major oxidized and nonoxidized products formed in the gas phase, the formation of these products can be deciphered. To start, it can be recalled from the Raman spectrum that 1,3-butadiene, toluene, and *m*-xylene are all formed within the HTPB matrix and are then released into the gas phase. As stated previously, molecules like 1,3-butadiene and toluene have been found to be prominent in HTPB decomposition.[9,10] Looking at the path to form ethylene, it can be deduced that it can form from the C−C bond breakage in 1,3-butadiene.[44] From understanding where the nonoxidized products are formed, it helps establish a foundation to where the oxidized products come from. A plausible pathway to form methyl vinyl ether is through the reaction of ethylene and the methoxy radical,[50] where the methoxy radical has been shown to play a key role in combustion reactions.[51,52] Methoxybenzene can be formed through the reaction between the phenyl radical and methanol as described in previous studies.[53] The phenyl radical has many probable pathways of formation. One such pathway is the hydrogen abstraction of benzene.[53] Benzene has been shown to form from HTPB,[44] making it a possible precursor to the formation of the molecules that are observed here. The methoxy radical can also form methanol with hydrogen abstraction as shown in the aforementioned studies.[52,54,55] Methanol can also directly form from the cleavage of the C−C bond at the terminal end leaving the CH_2OH radical, which upon hydrogen abstraction yields methanol.[44,52,55] Finally, Nitrobenzene can form from electrophilic substitution of NO_2 and benzene.[56]

It is evident in the emission spectra that boron plays a key role in the combustion of HTPB. Key atomic, radical, and closed-shell species were observed in the form of atomic boron (B), boron dioxide (BO_2), boron monoxide (BO) (radicals), and diatomic carbon (C_2). The BO_2 emissions are the most dominant features in the emission spectrum, which consequently partly masks the other features present. In the UV region, there are possible other features masked by the BO_2 emissions such as, methoxy radical and the hydroxyl radical.[14−16,18,57] Looking at the formation of BO, it has been previously studied that atomic boron reacts with molecular oxygen to form BO and atomic oxygen.[58] From there, it has been established from the molecular beam and combustion studies that BO rapidly oxidizes with molecular oxygen to form BO_2 and atomic oxygen.[18,58,59] Both of these reactions are highly exoergic (−306, −70 kJ mol^{-1})[60] reaching a high combustion temperature of 2,200 K. The generated thermal energy can drive the efficient oxidative decomposition of the parent HTPB molecule, whereas, in the absence of boron no ignition occurs, and temperature only reaches up to 900 K for pure HTPB (Figure 7).

https://doi.org/10.1021/acs.jpca.4c06979
J. Phys. Chem. A 2025, 129, 288−300

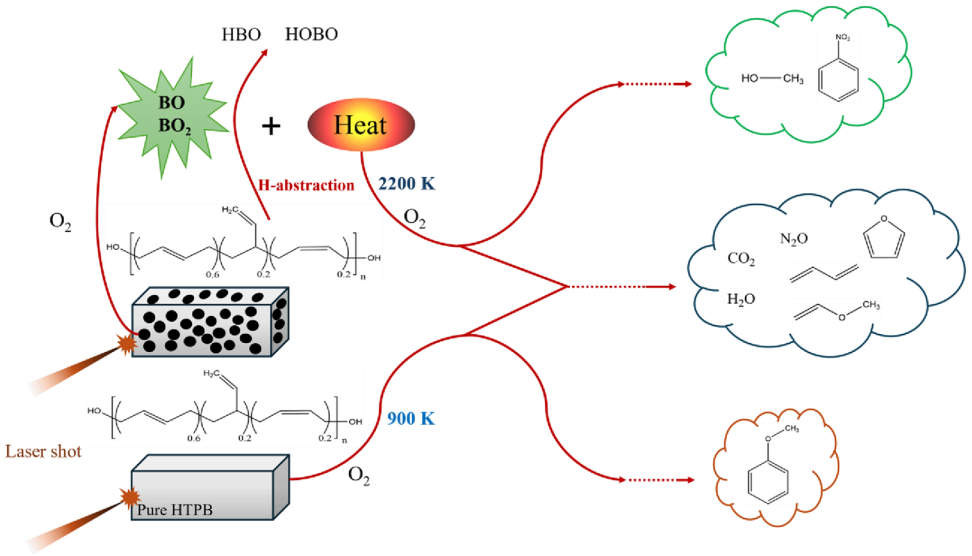

Figure 7. Reaction scheme of the major products formed during the heating and ignition of pure HTPB and B/HTPB in 20% O_2 and 80% Ar. Common products shared between the two materials are shown in blue. Shown in green are the exclusive products of the ignition of B/HTPB and in orange are the exclusive products formed from the heating of pure HTPB.

The role of thermal energy generated due to the oxidation of boron can be easily traced in the stronger CO_2 bands in the FT-IR spectra and denser smoke in the optical images for B/HTPB − overall, indicating a better combustion efficiency of the base fuel (HTPB). The boron oxides (BO and BO_2) can also directly abstract hydrogen from HTPB generating radical precursors, which can easily decompose to closed-shell hydrocarbons, as detected in the FT-IR spectra. Similar phenomena of hydrogen abstraction from another hydrocarbon fuel, *exo*-tetrahydrodicyclopentadiene (JP-10) forming highly reactive radicals have been shown earlier and they initiate the oxidation process of JP-10.[18] In that case, BO_2 hydrogen abstraction produces meta boric acid (HOBO) via a low-barrier (5 kJ mol^{-1}) exoergic reaction (−60 kJ mol^{-1}).[18] Boron hydride oxide (HBO) was found to be formed during the barrierless hydrogen abstraction of JP-10 by the BO radical producing an exoergic reaction (−74 kJ mol^{-1}).[18] These boron oxide-initiated pathways potentially drive the combustion of HTPB. Finally, C_2 originates from the hydrocarbon fuel at high temperatures and is known to be a common intermediate formed during the combustion processes.[15,18]

The vibrational temperatures revealed key insights into how the energy is dissipated throughout the ignition event. First looking at the vibrational temperature of the BO, it is observed that the temperature spikes in the initial stages of the ignition. For BO_2, the temperature stays consistent with little increase in the second stage of the ignition. This temperature stays the most consistent with the gray body temperature obtained during the experiment. Finally, C_2 is observed to have the most significant increase in temperature. This increase is most notable during the second stage of the ignition. The first electronically excited state ($A\ ^2\Pi$) of BO has a very long radiative lifetime of 1.5−1.6 μs.[61] Hence, during ignition, the population of electronically excited BO (BO*) is largely accumulated and the emission process to different excited vibrational levels in the electronic ground state ($X\ ^2\Sigma^+$) gets elongated resulting in vibrationally "hot" BO species, which explains the initial jump in the corresponding vibrational temperature. However, the lowering of this temperature with the progress of the ignition (beyond 30 ms) indicates a rapid decay of BO*. This phenomenon can be a manifestation of the oxidation of BO* in the high oxidative environment generating BO_2 via the following reaction (eq 2).[62]

$$BO^* + O_2 \rightarrow BO_2 + O \quad (2)$$

The dissipated energy can, in turn, excite BO_2, causing a rise in its vibrational temperature (Figure 6). However, the observed temperature increase is not as huge as BO, because the electronically excited $A\ ^2\Pi u$ state of BO_2 is rather short-lived (between 87 and 182 ns),[63] i.e., one order of magnitude shorter than that of BO. This short radiation lifetime allows a fast de-excitation of the energy to the electronic ground state ($X\ ^2\Pi g$) where, being a triatomic molecule, a greater number of vibrational modes facilitates the relaxation.[61,63] Hence, despite its predominant presence in the ignition (indicating high number density), the BO_2 vibrational temperature is not remarkably high.

The increase in the C_2 vibrational temperature during the second stage of the ignition is indicative of the HTPB combustion. The vibrational modes and structures are responsible for the differences between the vibrational temperatures of each species. All three species (C_2, BO, and BO_2) have linear structures; however, because BO_2 is triatomic, it has four modes of vibration, whereas BO and C_2 only have one. This indicates that BO_2 has more modes of vibration to easily disperse the energy. In other words, its density of states is much higher with increasing temperature, leading to an effective lower vibrational temperature than the other two diatomic species. Looking at C_2 and BO, they both only have one mode of vibration (stretching) which means that the structure alone cannot explain the increase in C_2 vibrational temperature. The vibrational temperature of C_2 is likely higher than BO due to C_2 being able to participate in intersystem crossing between the singlet and triplet states found in C_2 (d $^3\Pi g$ - a $^3\Pi u$).[64,65] Additionally, it is found that depletion of the excited state not only occurs due to the excitation to higher levels, leading to dissociation and ionization, but also by de-excitation to lower levels by fast quenching (approximately 7.95 × 10^{-11} cm^3 $molecules^{-1}$ s^{-1}).[66] Overall causing a net depletion of the

https://doi.org/10.1021/acs.jpca.4c06979
J. Phys. Chem. A 2025, 129, 288−300

excited state population in the higher vibrational levels, which explains the delayed high vibrational temperature in the second stage.[67]

5. CONCLUSIONS

In summary, here, through synchronized characterization techniques, it was determined that boron plays an important catalytic role in the ignition and decomposition of HTPB and essentially triggers the ignition of HTPB. The addition of boron was found to increase the production of gaseous products and produce hotter temperatures with less particle mass wastage. Additionally, boron upon fast oxidation yields reactive intermediates (BO and BO_2) that upon hydrogen abstraction from HTPB generate precursor radicals to finally form terminal products. The energy liberated in the initial oxidation of boron also eases the primary decomposition of HTPB, resulting in a highly efficient combustion of the hydrocarbon fuel. This study reveals a plausible mechanistic path for the thermal decomposition and ignition of B/HTPB via rigorous in situ identification of key transients and end products in the controlled, simulated environment. These key findings can ultimately aid in the production of next-generation solid rockets and hydrocarbon fuels.

■ ASSOCIATED CONTENT

Data Availability Statement

The data supporting this article have been included as part of the Supporting Information.

Supporting Information

The Supporting Information is available free of charge at https://pubs.acs.org/doi/10.1021/acs.jpca.4c06979.

Pulse sequence for decomposition and ignition studies; optical and infrared camera images for HTPB and B/HTPB in 100% Ar and 20% O_2/80% Ar; Raman spectra of HTPB in 100% Ar; Raman and FTIR peak assignment tables for HTPB and B/HTPB in 100% Ar and 20% O_2/80% Ar; emission spectra peak assignment tables for B/HTPB; 2D plot of B/HTPB emission spectra; emission profiles; combined gas phase FTIR spectra of B/HTPB and HTPB in 100% Ar (PDF)

Optical and infrared camera movies for HTPB in 100% Ar (M1 and M1IR), B/HTPB in 100% Ar (M2 and M2IR), HTPB in 20% O_2/80% Ar (M3 and M3IR), and B/HTPB in 20% O_2/80% Ar (M4 and M4IR) (ZIP)

■ AUTHOR INFORMATION

Corresponding Authors

Xiaolin Zheng − *Department of Mechanical Engineering, Stanford University, Stanford, California 94305-3032, United States;* orcid.org/0000-0002-8889-7873; Email: xlzheng@stanford.edu

Ralf I. Kaiser − *Department of Chemistry, University of Hawai'i at Manoa, Honolulu, Hawaii 96822, United States;* orcid.org/0000-0002-7233-7206; Email: ralfk@hawaii.edu

Authors

Grace L. Rizzo − *Department of Chemistry, University of Hawai'i at Manoa, Honolulu, Hawaii 96822, United States*

Souvick Biswas − *Department of Chemistry, University of Hawai'i at Manoa, Honolulu, Hawaii 96822, United States;* orcid.org/0000-0002-1643-2663

Dongwon Ka − *Department of Mechanical Engineering, Stanford University, Stanford, California 94305-3032, United States;* orcid.org/0000-0001-8194-7949

Complete contact information is available at: https://pubs.acs.org/10.1021/acs.jpca.4c06979

Notes

The authors declare no competing financial interest.

■ ACKNOWLEDGMENTS

The Hawaii group was supported by the United States Office of Naval Research (ONR) under contract number N00014-22-1-2010. X.Z. acknowledges the support by the Office of Naval Research managed by Chad Stoltz under agreement number N00014-22-1-2489.

■ REFERENCES

(1) Lehman, M. *Robert H. Goddard: Pioneer of Space Research;* Da Capo Press, Inc.: New York, NY, 1963.

(2) Jiang, Y.; Dincer Yilmaz, N. E.; Barker, K. P.; Baek, J.; Xia, Y.; Zheng, X. Enhancing Mechanical and Combustion Performance of Boron/Polymer Composites via Boron Particle Functionalization. *ACS Appl. Mater. Interfaces* **2021**, *13* (24), 28908−28915.

(3) Wang, Y. H.; Liu, L. L.; Xiao, L. Y.; Wang, Z. X. Thermal Decomposition of HTPB/AP and HTPB/HMX Mixtures with Low Content of Oxidizer. *J. Therm. Anal. Calorim.* **2015**, *119* (3), 1673−1678.

(4) Jiang, Y.; Leem, J.; Robinson, A. M.; Wu, S.; Huynh, A. H.; Ka, D.; Zhao, R. R.; Xia, Y.; Zheng, X. Tailoring the Mechanical and Combustion Performance of B/HTPB Composite Solid Fuel with Covalent Interfaces. *Compos. Sci. Technol.* **2024**, *245*, No. 110350.

(5) Lee, D.; Lee, C. Combustion Performance of a Staged Hybrid Rocket with Boron Addition. In *Journal of Physics: Conference Series*; IOP Publishing, 2018; Vol. *1005*, p 012035.

(6) Lu, J.; Chen, C.; Zhang, B.; Niu, K.; Xiao, F.; Liang, T. Combustion and Mechanical Properties Enhancement Strategy Based on Stearic Acid Surface Activated Boron Powders. *Sci. Rep.* **2024**, *14* (1), 21979.

(7) Pal, Y.; Mahottamananda, S. N.; Palateerdham, S. K.; Ingenito, A.; Trache, D. Oxidation Reaction Kinetics of HTPB-Boron Carbide/Polytetrafluoroethylene Formulations as a Solid Fuel. *Fuel* **2023**, *352*, No. 129042.

(8) Ka, D.; Baek, J.; Jiang, Y.; Huynh, A. H.; Gross, G. R.; Kong, D.; Xia, Y.; Zheng, X. Mechanical and Combustion Properties of Fluoroalkylsilane Surface-Functionalized Boron/HTPB Composite. *Combust. Flame* **2024**, *268*, No. 113621.

(9) Tian, J.; Zhu, H.; Li, R.; Cai, G. Insight into HTPB Pyrolysis Mechanism under High-Temperature: A Reactive Molecular Dynamics Study. *J. Anal. Appl. Pyrolysis* **2024**, *183*, No. 106789.

(10) Karpovych, V.; Kozliak, E.; Haiduk, N.; Sulkes, M. Short Timescale High Temperature Pyrolysis Products of Hydroxyl-Terminated Polybutadiene. *Fuel* **2023**, *343*, No. 127655.

(11) Jain, A.; Anthonysamy, S.; Ananthasivan, K.; Gupta, G. S. Studies on the Ignition Behaviour of Boron Powder. *Thermochim. Acta* **2010**, *500* (1−2), 63−68.

(12) Kuo, K. K.; Acharya, R. *Applications of Turbulent and Multiphase Combustion*; John Wiley and Sons: Hoboken, NJ, 2012.

(13) Yeh, C. L.; Kuo, K. K. Ignition and Combustion of Boron Particles. *Prog. Energy Combust. Sci.* **1996**, *22* (6), 511−541.

(14) Biswas, S.; Fujioka, K.; Antonov, I.; Rizzo, G. L.; Chambreau, S. D.; Schneider, S.; Sun, R.; Kaiser, R. I. Hypergolic Ionic Liquids: To Be or Not to Be? *Chem. Sci.* **2024**, *15* (4), 1480−1487.

(15) Antonov, I.; Chyba, A.; Perera, S. D.; Turner, A. M.; Pantoya, M. L.; Finn, M. T.; Epshteyn, A.; Kaiser, R. I. Discovery of Discrete Stages in the Oxidation of Exo-Tetrahydrodicyclopentadiene ($C_{10}H_{16}$) Droplets Doped with Titanium-Aluminum-Boron Reactive Mixed-Metal Nanopowder. *J. Phys. Chem. Lett.* **2022**, *13* (41), 9777−9785.

(16) Rizzo, G. L.; Biswas, S.; Pantoya, M. L.; Kaiser, R. I. Unraveling the Ignition Chemistry of Singly Levitated Aluminum Iodate Hexahydrate (AIH) Particles. *Chem. Phys. Lett.* **2024**, *842*, No. 141212.
(17) Rizzo, G. L.; Biswas, S.; Antonov, I.; Miller, K. K.; Pantoya, M. L.; Kaiser, R. I. Exotic Inverse Kinetic Isotopic Effect in the Thermal Decomposition of Levitated Aluminum Iodate Hexahydrate Particles. *J. Phys. Chem. Lett.* **2023**, *14* (11), 2722−2730.
(18) Brotton, S. J.; Perera, S. D.; Misra, A.; Kleimeier, N. F.; Turner, A. M.; Kaiser, R. I.; Palenik, M.; Finn, M. T.; Epshteyn, A.; Sun, B. J.; et al. Combined Spectroscopic and Computational Investigation on the Oxidation of Exo-Tetrahydrodicyclopentadiene (JP-10; $C_{10}H_{16}$) Doped with Titanium−Aluminum−Boron Reactive Metal Nanopowder. *J. Phys. Chem. A* **2022**, *126*, 125−144.
(19) Biswas, S.; Antonov, I.; Fujioka, K.; Rizzo, G. L.; Chambreau, S. D.; Schneider, S.; Sun, R.; Kaiser, R. I. Unraveling the Initial Steps of the Ignition Chemistry of the Hypergolic Ionic Liquid 1-Ethyl-3-Methylimidazolium Cyanoborohydride ([EMIM][CBH]) with Nitric Acid (HNO_3) Exploiting Chirped Pulse Triggered Droplet Merging. *Phys. Chem. Chem. Phys.* **2023**, *25* (9), 6602−6625.
(20) Paul, D.; Biswas, S.; Yeom, H.; Na, K.; Pantoya, M. L.; Kaiser, R. I. Unraveling the Nanosheet Zeolite-Catalyzed Combustion of Aluminum Nanoparticles-Doped Exo-Tetrahydrodicyclopentadiene (JP-10) Energetic Fuel. *ACS Appl. Mater. Interfaces* **2024**, *16* (40), 53938−53949.
(21) Chase, M. W. *J. NIST-JANAF Themochemical Tables*, Fourth ed.; American Chemical Society: Washington DC, 1998.
(22) Risha, G. A.; Ulas, A.; Boyer, E.; Kumar, S.; Kuo, K. K. Combustion of HTPB-Based Solid Fuels Containing Nano-Sized Energetic Powder in a Hybrid Rocket Motor. In *37th Joint Propulsion Conference and Exhibit*; American Institute of Aeronautics and Astronautics Inc.: Salt Lake City, UT, 2001; pp 2001−3535.
(23) Chaves, F. R.; Góis, J. C. Research on the Specific Heat Capacity of PBX Formulations Based on RDX. *J. Aerosp. Technol. Manag.* **2016**, *8* (3), 352−356.
(24) Cornell, S. W.; Koenig, J. L. The Raman Spectra of Polybutadiene Rubbers. *Macromolecules* **1969**, *2* (5), 540−545.
(25) Wilmshurst, J. K.; Bernstein, H. J. THE INFRARED AND RAMAN SPECTRA OF TOLUENE, TOLUENE-α-D3, m-XYLENE, AND m-XYLENE-Aα'-D6. *Can. J. Chem.* **1957**, *35*, 911−925.
(26) Lindenmaier, R.; Scharko, N. K.; Tonkyn, R. G.; Nguyen, K. T.; Williams, S. D.; Johnson, T. J. Improved Assignments of the Vibrational Fundamental Modes of Ortho-, Meta-, and Para-Xylene Using Gas- and Liquid-Phase Infrared and Raman Spectra Combined with Ab Initio Calculations: Quantitative Gas-Phase Infrared Spectra for Detection. *J. Mol. Struct.* **2017**, *1149*, 332−351.
(27) Socrates, G. *Infrared and Raman Characteristic Group Frequencies: Tables and Charts*, Third.; John Wiley & Sons, Ltd: England, Chichester, 2001.
(28) Nallasamy, P.; Anbarasan, P. M.; Mohan, S. Vibrational Spectra and Assignments of cis- and Trans-1,4-Polybutadiene. *Turk. J. Chem.* **2002**, *26*, 105−111.
(29) Craig, N. C.; Davis, J. L.; Hanson, K. A.; Moore, M. C.; Weidenbaum, K. J.; Lock, M. Analysis of the Rotational Structure in Bands in the High-Resolution Infrared Spectra of Butadiene and Butadiene-2,3-D2: Refinement in Assignments of Fundamentals. *J. Mol. Struct.* **2004**, *695*−*696*, 59−69.
(30) Margoshes, M.; Fassel, V. A. The infrared spectra of aromatic compounds: I. The out-of-plane C-H bending vibrations in the region 625−900 cm−1. *Spectrochim. Acta* **1955**, *7*, 14−24.
(31) Chen, J. K.; Brill, T. B. Chemistry and Kinetics of Hydroxyl-Terminated Polybutadiene (HTPB) and Diisocyanate-HTPB Polymers during Slow Decomposition and Combustion-like Conditions. *Combust. Flame* **1991**, *87* (3−4), 217−232.
(32) Liang, J.; Nie, J.; Zhang, H.; Guo, X.; Yan, S.; Han, M. Interaction Mechanism of Composite Propellant Components under Heating Conditions. *Polymer* **2023**, *15* (11), 2485.
(33) Ducruet, N.; Delmotte, L.; Schrodj, G.; Stankiewicz, F.; Desgardin, N.; Vallat, M. F.; Haidar, B. Evaluation of Hydroxyl Terminated Polybutadiene-Isophorone Diisocyanate Gel Formation During Crosslinking Process. *J. Appl. Polym. Sci.* **2013**, *128* (1), 436−443.
(34) Shimanouchi, T. *Tables of Molecular Vibrational Frequencies*, Consolidated Vol. I; National Bureau of Standards: Washington, DC, 1972.
(35) Burcl, R.; Handy, N. C.; Carter, S. Vibrational Spectra of Furan, Pyrrole, and Thiophene from a Density Functional Theory Anharmonic Force Field. *Spectrochim. Acta Part A Mol. Biomol. Spectrosc.* **2003**, *59* (8), 1881−1893.
(36) Cataliotti, R.; Paliani, G. Infrared Study of the C-H Stretching Region of Five-Membered Heterocyclic Compounds. *Can. J. Chem.* **1976**, *54*, 2451−2457.
(37) Owen, N. L.; Hester, R. E. Vibrational Spectra and Torsional Barriers of Anisole and Some Monohalogen Derivatives. *Spectrochim. Acta Part A Mol. Spectrosc.* **1969**, *25* (2), 343−354.
(38) Stephenson, C. V.; Coburn, W. C.; Wilcox, W. S. The Vibrational Spectra and Assignments of Nitrobenzene, Phenyl Isocyanate, Phenyl Isothiocyanate, Thionylaniline and Anisole. *Spectrochim. Acta* **1961**, *17* (9−10), 933−946.
(39) Ignatyev, I. S.; Lazarev, A. N.; Smirnov, M. B.; Alpert, M. L.; Trofimov, B. A. Vibrational Spectra and Molecular Structure of Methyl Vinyl Ether. *J. Mol. Struct.* **1981**, *72* (C), 25−39.
(40) Ignatyev, I. S.; Montejo, M.; Sundius, T.; Partal Ureña, F.; López González, J. J. Structure and Vibrational Spectra of Vinyl Ether Conformers. The Comparison of B3LYP and MP2 Predictions. *Chem. Phys.* **2007**, *333* (2−3), 148−156.
(41) Falk, M.; Whalley, E. Infrared Spectra of Methanol and Deuterated Methanols in Gas, Liquid, and Solid Phases. *J. Chem. Phys.* **1961**, *34* (5), 1554−1568.
(42) Clarkson, J.; Smith, W. E. A DFT Analysis of the Vibrational Spectra of Nitrobenzene. *J. Mol. Struct.* **2003**, *655* (3), 413−422.
(43) Laane, J.; Ohlsen, J. R. *Characterization of Nitrogen Oxides by Vibrational Spectroscopy*; Lippard, S. J., Ed.; John Wiley & Sons, Ltd, 1980.
(44) Qian, Y.; Wang, Z.; Chen, L.; Liu, P.; Jia, L.; Dong, B.; Li, H.; Xu, S. A Study on the Decomposition Pathways of HTPB and HTPE Pyrolysis by Mass Spectrometric Analysis. *J. Anal. Appl. Pyrolysis* **2023**, *170*, No. 105929.
(45) Ge, Y. H.; Kang, J. Y.; Zhou, J. H.; Shi, L. W. Theoretical Investigation on Thermal Aging Mechanism and the Aging Effect on Mechanical Properties of HTPB−IPDI Polyurethane. *Comput. Mater. Sci.* **2016**, *115*, 92−98.
(46) Hashim, S. A.; Karmakar, S.; Roy, A. Combustion Characteristics of Boron-HTPB-Based Solid Fuels for Hybrid Gas Generator in Ducted Rocket Applications. *Combust. Sci. Technol.* **2019**, *191* (11), 2082−2100.
(47) Chen, B.; Xia, Z.; Huang, L.; Hu, J. Ignition and Combustion Model of a Single Boron Particle. *Fuel Process. Technol.* **2017**, *165*, 34−43.
(48) Shankar, R. M.; Roy, T. K.; Jana, T. Terminal Functionalized Hydroxyl-Terminated Polybutadiene: An Energetic Binder for Propellant. *J. Appl. Polym. Sci.* **2009**, *114* (2), 732−741.
(49) Zielinkiewicz, K.; Baranowska, D.; Mijowska, E. Ball Milling Induced Borophene Flakes Fabrication. *RSC Adv.* **2023**, *13* (25), 16907−16914.
(50) Lissi, E. A.; Massiff, G.; Villa, A. Addition of Methoxy Radicals to Olefins. *Int. J. Chem. Kinet.* **1975**, *7* (4), 625−631.
(51) Bofill, J. M.; Olivella, S.; Solé, A.; Anglada, J. M. The Mechanism of Methoxy Radical Oxidation by O_2 in the Gas Phase. Computational Evidence for Direct H Atom Transfer Assisted by an Intermolecular Noncovalent O···O Bonding Interaction. *J. Am. Chem. Soc.* **1999**, *121* (6), 1337−1347.
(52) Yalamanchi, K. K.; Bai, X.; Fernando, N. D.; Lua, A. S.; Cheng, S.; Li, Y.; Zhou, C.-W.; Goldsborough, S. S.; Sarathy, S. M. From Electronic Structure to Model Application of Key Reactions for Gasoline/Alcohol Combustion: Hydrogen-Atom Abstractions by $CH_3\dot{O}$ Radical. *Combust. Flame* **2023**, *252*, No. 112742.
(53) Mondal, K.; Kaipara, R.; Rajakumar, B. Investigation of the Absorption Cross Section of Phenyl Radical and Its Kinetics with

https://doi.org/10.1021/acs.jpca.4c06979
J. Phys. Chem. A 2025, 129, 288−300

Methanol in the Gas Phase Using Cavity Ring-Down Spectroscopy and Theoretical Methodologies. *J. Phys. Chem. A* **2019**, *123* (45), 9682−9692.
(54) Rahmawati, I.; Yetri, N. Y.; Gunlazuardi, J.; Ivandini, T. A. Electroreduction of CO_2 Using Modified Boron-Doped Diamond Electrode as the Working Electrode. *IOP Conf. Ser. Mater. Sci. Eng.* **2020**, *902* (1), No. 012011.
(55) Wang, J.; Marks, J. H.; Turner, A. M.; Nikolayev, A. A.; Azyazov, V.; Mebel, A. M.; Kaiser, R. I. Mechanistical Study on the Formation of Hydroxyacetone (CH_3COCH_2OH), Methyl Acetate (CH_3COOCH_3), and 3-Hydroxypropanal ($HCOCH_2CH_2OH$) along with Their Enol Tautomers (Prop-1-Ene-1,2-Diol ($CH_3C(OH)CHOH$), Prop-2-Ene-1,2-Diol ($CH_2C(OH)CH_2OH$), 1-Methoxyethen-1. *Phys. Chem. Chem. Phys.* **2023**, *25* (2), 936−953.
(56) Polášek, M.; Tureček, F. Hydrogen Atom Adducts to Nitrobenzene: Formation of the Phenylnitronic Radical in the Gas Phase and Energetics of Wheland Intermediates. *J. Am. Chem. Soc.* **2000**, *122* (39), 9511−9524.
(57) Ohbayashi, K.; Akimoto, H.; Tanaka, I. Emission Spectra of CH_3O, C_2H_5O, and i-C_3H_7O Radicals. *J. Phys. Chem.* **1977**, *81* (8), 798−802.
(58) Hashim, S. A.; Ojha, P. K.; Karmakar, S.; Roy, A.; Chaira, D. Experimental Observation and Characterization of B−HTPB-Based Solid Fuel with Addition of Iron Particles for Hybrid Gas Generator in Ducted Rocket Applications. *Propellants, Explos. Pyrotech.* **2019**, *44* (7), 896−907.
(59) Maksyutenko, P.; Parker, D. S. N.; Zhang, F.; Kaiser, R. I. An LIF Characterization of Supersonic BO ($X^2\Sigma^+$) and CN ($X^2\Sigma^+$) Radical Sources for Crossed Beam Studies. *Rev. Sci. Instrum.* **2011**, *82* (8), No. 083107.
(60) Johnson, R. D. *NIST Computational Chemistry Comparison and Benchmark Database* http://cccbdb.nist.gov/
(61) Zhang, J.; Li, H.; Ma, Y.; Zhu, Z. Investigations on Transition Properties of $X^2\Sigma^+$, $A^2\Pi$, $B^2\Sigma^+$, $C^2\Pi$, and $A^4\Sigma^+$ States, and Their Ω States of BO. *J. Quant. Spectrosc. Radiat. Transfer* **2021**, *272*, No. 107762.
(62) Balucani, N.; Zhang, F.; Kaiser, R. I. Elementary Reactions of Boron Atoms with Hydrocarbons - Toward the Formation of Organo-Boron Compounds. *Chem. Rev.* **2010**, *110* (9), 5107−5127.
(63) Hodgson, A. The $A^2\Pi u$ State of BO_2. Radiative Lifetime, Electronic Quenching and Coupling with $X^2\Pi g$. *J. Chem. Soc. Faraday Trans. 2 Mol. Chem. Phys.* **1985**, *81* (9), 1445−1461.
(64) Wehres, N.; Romanzin, C.; Linnartz, H.; Van Winckel, H.; Tielens, A. G. G. M. C_2 Emission Features in the Red Rectangle - A Combined Observational/Laboratory Study. *Astron. Astrophys.* **2010**, *518* (17), A36.
(65) Nakajima, M.; Endo, Y. Spectroscopic Observation of Higher Vibrational Levels of C_2 through Visible Band Systems. *J. Chem. Phys.* **2013**, *139* (24), No. 244310.
(66) Smith, G. P.; Park, C.; Schneiderman, J.; Luque, J. C_2 Swan Band Laser-Induced Fluorescence and Chemiluminescence in Low-Pressure Hydrocarbon Flames. *Combust. Flame* **2005**, *141* (1−2), 66−77.
(67) Harilal, S. S.; Issac, R. C.; Bindhu, V.; Nampoori, P. N.; Vallabhan, G. Optical Emission Studies of C_2 Species in Laser-Produced Plasma from Carbon. *J. Phys. D Appl. Phys.* **1997**, *30*, 1703−1709.

https://doi.org/10.1021/acs.jpca.4c06979
J. Phys. Chem. A 2025, 129, 288−300